Efficient exact exchange using Wannier functions and other related developments in planewave-pseudopotential implementation of RT-TDDFT

Cite as: J. Chem. Phys. 161, 024111 (2024); doi: 10.1063/5.0211238

Submitted: 29 March 2024 • Accepted: 19 June 2024 •

Published Online: 10 July 2024







Christopher Shepard, DRuiyi Zhou, DJohn Bost, DThomas E. Carney, DYi Yao, Christopher Shepard, DRUIYI Zhou, DJohn Bost, DThomas E. Carney, DYI Yao, Christopher Shepard, DRUIYI Zhou, DJohn Bost, DJohn Bost, DThomas E. Carney, DYI Yao, DANIEL CARNES, DANIEL CARNE

AFFILIATIONS

- Department of Chemistry, University of North Carolina at Chapel Hill, Chapel Hill, North Carolina 27599, USA
- ²Thomas Lord Department of Mechanical Engineering and Materials Science, Duke University, Durham, North Carolina 27708, USA
- ³Department of Physics and Astronomy, University of North Carolina at Chapel Hill, Chapel Hill, North Carolina 27599, USA

ABSTRACT

The plane-wave pseudopotential (PW-PP) formalism is widely used for the first-principles electronic structure calculation of extended periodic systems. The PW-PP approach has also been adapted for real-time time-dependent density functional theory (RT-TDDFT) to investigate time-dependent electronic dynamical phenomena. In this work, we detail recent advances in the PW-PP formalism for RT-TDDFT, particularly how maximally localized Wannier functions (MLWFs) are used to accelerate simulations using the exact exchange. We also discuss several related developments, including an anti-Hermitian correction for the time-dependent MLWFs (TD-MLWFs) when a time-dependent electric field is applied, the refinement procedure for TD-MLWFs, comparison of the velocity and length gauge approaches for applying an electric field, and elimination of long-range electrostatic interaction, as well as usage of a complex absorbing potential for modeling isolated systems when using the PW-PP formalism.

Published under an exclusive license by AIP Publishing. https://doi.org/10.1063/5.0211238

I. INTRODUCTION

In recent decades, the explicit real-time propagation approach to time-dependent density functional theory (RT-TDDFT)¹⁻⁵ has garnered substantial interest as a powerful approach for investigating time-dependent electron dynamics. While linear response (LR)-TDDFT⁶ has long established itself for studying optical excitation,^{7,8} RT-TDDFT has further expanded the applicability of TDDFT⁹ for the investigation of various nonequilibrium dynamics of electrons. Beyond its broader utility for studying both linear and nonlinear responses to external perturbations on equal footing,¹⁰ RT-TDDFT is an attractive approach even for the optical absorption spectrum of large extended systems because of how its computational cost scales. ¹¹⁻¹³ With its appealing balance between accuracy and computational cost, along with access to the

time-dependent nonequilibrium electron density, RT-TDDFT has proven invaluable in investigating a myriad of excited state phenomena such as optical absorption, ^{14,15} electronic stopping, ^{16–22} electronic circular dichroism spectra, ^{10,23} topological quantum matter, ^{24–26} and high harmonic generation. ^{27,28} The popularity of RT-TDDFT has led to its implementation in a variety of electronic structure codes, including SALMON, ²⁹ SIESTA, ^{30,31} CP2K, ³² GAUSSIAN, ^{33,34} Q-Chem, ^{35,36} NWChem, ^{37,38} Octopus, ^{39,40} TDAP, ^{41,42} INQ, ⁴³ and Qbox/Qb@ll. ^{44–47} Implementation details vary greatly by code, particularly in terms of the basis set used, ranging from real-space grids, Gaussian-type orbitals, numeric atomic-orbitals, to plane-waves (PW).

The plane-wave pseudopotential (PW-PP) implementation, utilizing plane-waves (PW) as the basis set and non-local pseudopotentials to reproduce core electron effects, 48,49 has a long history

a) Author to whom correspondence should be addressed: ykanai@unc.edu

in studies of extended periodic systems, ^{50–52} with several implementations of the RT-TDDFT method using this formalism, such as the Qb@ll version of the Qbox code. ^{4,47} The PW-PP formalism is particularly convenient when the electronic excitation exhibits an ionization character because the PW basis functions are independent of the locations of the atomic nuclei. At the same time, the use of modern exchange-correlation (XC) functionals requiring exact exchange (EXX) becomes computationally prohibitive in the PW-PP implementation. ⁵³ Studying isolated systems like molecules using the PW-PP approach is also not always straightforward, unlike for calculations of ground-state properties, as briefly mentioned in Ref 12

In this work, we report recent advances on a few key aspects of the PW-PP implementation for the RT-TDDFT method. We discuss how the unitary transformation to maximally localized Wannier functions (MLWFs) can be used to reduce the computational cost of the exact exchange by recognizing the nearsightedness principle of electrons. 54,55 Such an approach has been previously demonstrated in the context of first-principles molecular dynamics (FPMD) simulation,⁵⁶ and we extend the idea to RT-TDDFT simulation. We showcase the efficiency of this approach by calculating the absorption spectra of extended periodic systems, first with crystalline silicon and then with the one-dimensional hydrogen chain system, which is often used to test XC functionals. We further introduce an anti-Hermitian correction for preserving the orthonormality of the time-dependent MLWFs (TD-MLWFs), which becomes a practical concern when an electric field is applied through the length gauge (LG) in real-time simulations of extended systems. We subsequently extend the refinement approach of Stengel and Spaldin⁵⁷ to TD-MLWFs and illustrate how their refinement scheme can be used to accelerate the convergence of the calculation of absorption spectra with respect to simulation cell size. Importantly, we also address the question of gauge invariance for the application of electric field to an extended system within the PW-PP formalism in the context of RT-TDDFT, comparing the length and velocity gauges (VGs). We compare the results using the conventional velocity gauge and the length gauge (using TD-MLWFs) to represent the external electromagnetic field. This is particularly informative because the use of non-local pseudopotentials, strictly speaking, violates this gauge invariance.⁵⁸ Finally, we address numerical complications that arise when modeling nonequilibrium electron excitation in isolated systems using the PW-PP formalism. All the developments are implemented with the Ob@ll version of the Obox code, a massively parallel open-source code written in C++. 4,47 As the Qb@ll version is no longer updated, the new implementations discussed here are available under a new forked version, Qb@ch.59

II. EFFICIENT EXACT EXCHANGE FOR REAL-TIME PROPAGATION

Given the great popularity of density functional theory (DFT) in various areas of computational sciences at present, the development of increasingly accurate and efficient exchange-correlation (XC) functionals for Kohn–Sham (KS) DFT $^{60-62}$ is an important scientific endeavor with substantial potential impacts. For ground-state DFT calculations, highly sophisticated XC approximations such as those based on the exact exchange (EXX) and the random phase

approximation (RPA) for the correlation have been utilized with great success. 63-66 While the computational cost of these "non-standard" XC functionals, especially those on the fifth rung of the so-called Jacob's ladder of DFT, 67,68 remains prohibitive for most applications, we are hopeful as we continue to witness great advances in computing hardware. At the same time, the use of advanced XC functionals is much more restricted for TDDFT, especially for RT-TDDFT methods. For RT-TDDFT simulations of complex extended systems, the local-density approximation (LDA)69 and semi-local generalized gradient approximation (GGA) functionals such as Perdew–Burke–Ernzerhof (PBE)70 remain dominant, particularly for the PW-PP implementation. Meta-GGA functionals, which incorporate the kinetic energy density into the XC approximation, 71,72 have become more prevalent over the past decade and are actively being examined and improved. 73

Hybrid XC functionals, incorporating some fraction of exact exchange, have been shown to improve key quantities such as binding energies^{74,75} and bandgaps, 76,77</sup> and akin to DFT, many RT-TDDFT applications have shown improved results when using hybrid XC functionals, including those focused on charge transfer and optical properties. 37,78-80 However, calculation of the EXX for extended systems presents a high (and sometimes insurmountable) computational cost, particularly for the PW-PP formalism in which the basis sets are not spatially localized (thus unable to benefit from the long history of clever techniques like the resolution-of-identity81), and the delocalized nature of the KS orbitals makes the evaluation of the exchange integrals very time consuming. Additionally, with the need for small (atto-second) time steps in RT-TDDFT simulations, studies that require anything more than a few femtoseconds (fs), such as the calculation of optical absorption spectra, quickly become inaccessible. Recent work by Lin and co-workers has shown that utilizing the so-called parallel transport gauge accelerates PW-PP based RT-TDDFT simulations by limiting the oscillations of the KS orbitals. This allows for larger time steps, reducing the number of times the EXX integrals need to be calculated.⁸² When paired with the adaptively compressed exchange (ACE) operator method, which simultaneously lowers (compresses) the rank of the exchange operator to limit the cost of each step,^{53,83} additional acceleration was observed for large

Here we demonstrate how transforming the KS orbitals into an alternative gauge, the maximally localized Wannier functions (MLWFs) gauge, can also be used to achieve similar acceleration in RT-TDDFT simulations of extended systems that utilize hybrid XC functionals. At the heart of the RT-TDDFT simulation, the time-dependent Kohn–Sham (TD-KS) equation reads

$$i\frac{d}{dt}|\psi_n(t)\rangle = \left\{-\frac{1}{2}\nabla_{\mathbf{r}}^2 + \hat{v}_{ext}(\mathbf{r},t) + \int d\mathbf{r}' \frac{\rho(\mathbf{r}',t)}{|\mathbf{r}-\mathbf{r}'|} + \hat{v}_{XC}(\mathbf{r},t)\right\}|\psi_n(t)\rangle,\tag{1}$$

where $\psi_n(\mathbf{r},t)$ are the time-dependent single-particle Kohn–Sham orbitals and $\rho(\mathbf{r}',t)$ is the electron density. The external potential, \hat{v}_{ext} , accounts for all external potentials acting on the electrons, and \hat{v}_{XC} is the XC potential. The $-\frac{1}{2}\nabla_{\mathbf{r}}^2$ term is the kinetic energy operator, represented as \hat{T} in the following, and $\int d\mathbf{r}' \frac{\rho(\mathbf{r}',t)}{|\mathbf{r}-\mathbf{r}'|} = \hat{v}_H[\rho(\mathbf{r},t)]$ is

the Hartree potential. The corresponding Kohn-Sham Hamiltonian

$$\hat{H}(t) = \hat{T} + \hat{v}_{ext}(\mathbf{r}, t) + \hat{v}_{H}[\rho(\mathbf{r}, t)] + \hat{v}_{XC}[\{\psi_{n}(\mathbf{r}, t)\}].$$
 (2)

We assume there is no vector potential in the Hamiltonian for simplicity. For hybrid XC functionals, the exchange-correlation potential can be generally written as

$$\hat{v}_{XC}[\{\psi_n(\mathbf{r},t)\}] = (1-\alpha) \cdot \hat{v}_X[\rho(\mathbf{r},t)] + \alpha \cdot \hat{v}_X^{EXX}[\{\psi_n(\mathbf{r},t)\}] + \hat{v}_C[\rho(\mathbf{r},t)], \quad (3)$$

where \hat{v}_X and \hat{v}_C are the exchange and correlation potentials from a local or semi-local functional, respectively. \hat{v}_X^{EXX} is the exact exchange, and α is the mixing fraction for the exact exchange. The energy expression in RT-TDDFT⁴⁷ now contains the exact exchange energy,

$$E_X^{EXX}(t) = -\frac{1}{2} \sum_{ij} \iint \frac{\psi_i^*(\mathbf{r}',t)\psi_j(\mathbf{r}',t)\psi_i(\mathbf{r},t)\psi_j^*(\mathbf{r},t)}{|\mathbf{r} - \mathbf{r}'|} d\mathbf{r} d\mathbf{r}'. \quad (4)$$

For isolated molecules, increased accuracy has made the use of hybrid XC functionals quite common, as calculating the EXX is not prohibitive, even within the PW-PP formalism. We demonstrate this by calculating the absorption spectra of gas-phase water, where hybrid functionals, as expected, show much better agreement with experimental results (see Fig. S1 in the supplementary material). For extended periodic systems, however, the TD-KS orbitals take the form of Bloch states, and as a result, every orbital pair in Eq. (4) needs to be evaluated at each time step of the RT-TDDFT simulation, leading to a significant increase in computational cost. While many approaches have been proposed for reducing the cost of EXX computation when atom-centered basis functions are used,5 the PW-PP implementation requires a different solution. 53,83,84 We exploit the gauge freedom of the TD-KS orbitals, as any unitary transformation that preserves the electron density of the system will preserve the physical properties of the system, and employ the MLWF gauge. 85 Previous work with DFT86 and first-principles molecular dynamics (FPMD)⁵⁶ has utilized the spatial localization of MLWFs for efficient calculations using hybrid XC functionals, and we extend the idea to RT-TDDFT simulations using TD-MLWFs. 4,12 TD-MLWFs tend to remain highly localized, even in RT-TDDFT simulations, and minimal overlap is expected for distant TD-MLWFs in large systems. Exploiting the spatially localized exchange interaction of electrons in a localized representation we define a cutoff distance (denoted R_{cutoff}) based on the geometric centers of the TD-MLWFs such that the exact exchange integral is calculated only for the orbital pairs within the specified distance. Therefore, the exact exchange potential, $\hat{v}_X^{EXX}(t)$, applied to the Wannier function $w_i(\mathbf{r},t)$ can be defined as

$$\hat{v}_X^{EXX}(t)w_i(\mathbf{r},t) = -\sum_j \int \frac{w_j^*(\mathbf{r}',t)w_i(\mathbf{r}',t)}{|\mathbf{r}-\mathbf{r}'|}w_j(\mathbf{r},t)d\mathbf{r}', \quad (5)$$

such that the integrand is non-zero when

$$|\langle w_i | \hat{\mathbf{r}} | w_i \rangle| - |\langle w_j | \hat{\mathbf{r}} | w_j \rangle| < R_{cutoff}. \tag{6}$$

Here, the position operator $\hat{\mathbf{r}}$ is defined to be compatible with extended systems as87

$$\langle \hat{\mathbf{r}} \rangle = \frac{\mathbf{L}}{2\pi} \operatorname{Im} \ln \langle \psi | e^{i\frac{2\pi}{\mathbf{L}} \cdot \hat{\mathbf{r}}} | \psi \rangle, \tag{7}$$

where L is the lattice vector of the periodic simulation cell.⁸⁸ By eliminating the calculation of integrals that contribute minimally to the total EXX, the cost of employing hybrid XC functionals for extended systems can be significantly reduced without sacrificing accuracy, as demonstrated in the following two applications.

A. Demonstration 1: Crystalline silicon

Particularly when studying extended systems that require a large simulation cell, the reduction in computational cost through the use of MLWFs becomes increasingly significant. We demonstrate such an advantage by calculating the optical absorption spectrum of crystalline silicon using a large simulation cell. Here we employ the popular hybrid XC functional approximation PBE0.89 First, we determine the smallest R_{cutoff} , which can be used for an accurate evaluation of the EXX when using MLWFs. We expect this R_{cutoff} to be largely independent of the simulation cell size, but rather a material-specific property. 54,55 To determine R_{cutoff} , we utilized a 128-atom silicon cell elongated in the x-direction by repeating a small 8-atom supercell 16 times. To generate the absorption spectra, we applied a delta kick, in the form of an 0.001 a.u. electric field, in the x-direction to the ground-state MLWFs. The electric field was then turned off, and the TD-MLWFs were propagated for an additional 250 a.u. using a 0.05 a.u. time step and the enforced time-reversal symmetry propagator (ETRS) propagator. 90 This sudden delta kick of the electric field induces a phase in the wavefunctions, causing oscillations of the TD-MLWFs, which in turn can be used to calculate the electric dipole. The electric dipole is subsequently used to calculate the macroscopic current, which is then used to determine the imaginary part of the dielectric function (optical absorption for extended systems), as detailed in our previous work (Ref. 12). Simulations here were performed using a 15 Ry. cutoff for the kinetic energy in the plane-wave expansion of the TD-KS orbitals, and all atoms were represented by Hamann-Schluter-Chiang-Vanderbilt (HSCV) norm-conserving pseudopotentials.⁹¹ Figure 1 shows how the cutoff distance affects the computed absorption spectra for the small 128-atom (512 electron) simulation cell, and that computed spectrum remains unchanged until the cutoff distance is reduced below 15 bohrs.

Next, using the cutoff of 15 bohrs, we then calculated the optical absorption spectrum of crystalline silicon by employing a 2048-atom (8192 electron) simulation cell [see Fig. 2(a)]. This simulation cell size was determined to be fully converged with respect to the cell size (see Fig. S2 in the supplementary material), and with the cutoff, only 4.06% of EXX pairs are needed for this PBE0 calculation. An electric field with an amplitude of 0.001 a.u. was applied in the x-direction for 0.2 a.u. time to excite the system. The electric field was subsequently turned off, and the system was propagated in the MLWF gauge for an additional 225 a.u. using a 0.2 a.u. time step, the ETRS⁹⁰ propagator, and a plane-wave kinetic energy cutoff of 15 Ry. The cutoff energy of 15 Ry. was found to be large enough to give a converged result (see Fig. S3 in the supplementary

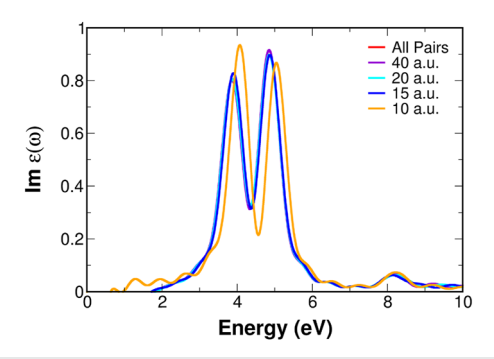


FIG. 1. Absorption spectra for a 128-atom crystalline silicon cell for varying MLWF cutoff distances (R_{cutoff}) using the PBE0 XC functional.

material). Termination of the numerical simulation leads to artificial "wiggles" in the absorption spectra. To remove these wiggles, we applied a damping function in the Fourier transform of the current, $f(t) = e^{-\beta t}$, using $\beta = 150$ as the damping coefficient. As seen in Fig. 2(b), the cutoff significantly reduces the computational cost of the PBE0 calculation by an order of magnitude. In this RT-TDDFT simulation with 8192 electrons, the PBE0 hybrid XC approximation is only 12 times more expensive than the standard semi-local PBE XC approximation. Figure 2(c) shows the resulting PBE0 absorption spectra, along with those of LDA, and the experimental spectra for comparison. Yhile PBE0 offers a significant improvement over the reference LDA spectrum, as it shifts the higher energy peak to the same position as the experimental spectra, the lower energy peak is still severely underestimated. Nonetheless, we demonstrate

here that the EXX reduction method based on the MLWFs allows us to perform large-scale RT-TDDFT simulations with hybrid XC approximations.

B. Demonstration 2: Hydrogen chain

Let us now discuss how our ability to perform RT-TDDFT simulation of extended systems with hybrid XC approximations helps to improve the description. In particular, we examine the case of the one-dimensional infinite chain of hydrogen atoms. The hydrogen chain is often used as a test system for studying excitonic effects in the absorption spectra of extended systems, as the physical properties significantly depend on the bond distances between hydrogen atoms. ⁹³ We first consider a chain with alternating bond distances of 2.0 and 2.5 a.u. with the geometry shown in Fig. 3(a). At this spacing, the chain is known to exhibit a strongly bound exciton, a feature whose accurate description often requires XC approximations beyond the semi-local approximation. ^{94,95} By using the TD-MLWF cutoff scheme outlined earlier, we employ several hybrid XC functionals to compute the optical absorption spectrum and compare them directly to local and semi-local XC functionals.

To obtain the absorption spectrum, a 0.001 a.u. delta kick in the form of an electric field was applied in the x-direction for 0.05 a.u. time to the system. The electric field was subsequently turned off, and the system was propagated in the MLWF gauge using the ETRS propagator of for an additional 400 a.u. time and a 0.05 a.u. time step. All spectra use the damping function $f(t) = e^{-\beta t}$ with $\beta = 150$, as discussed earlier. A plane-wave cutoff of 30 Ry was used, and a simulation cell of $522 \times 20 \times 20$ bohrs, consisting of 116 H_2 units, was sufficient for avoiding periodic interactions in the y and z directions.

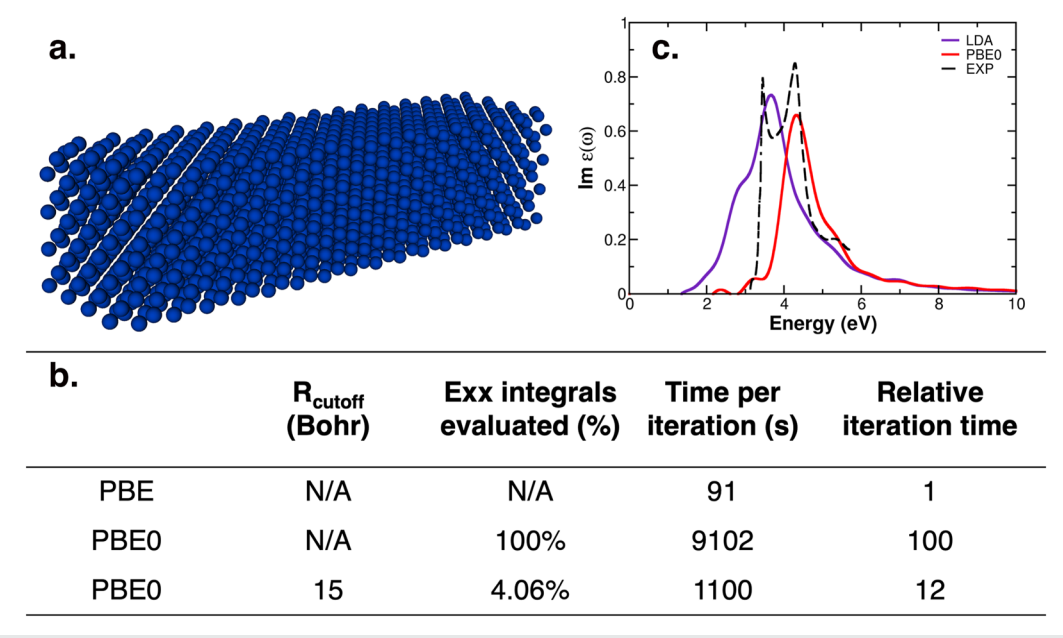


FIG. 2. (a) The 2048 atom crystalline silicon structure used to model the absorption spectra. (b) Computational cost of the PBE0 functional, relative to PBE, both with and without the MLWF cutoff scheme. Simulations were performed on ALCF-Theta using 32 768 processors (512 KNL nodes) and only MPI. (c) Optical absorption spectra of crystalline silicon using LDA and PBE0. The experimental spectrum is provided for comparison.⁹²

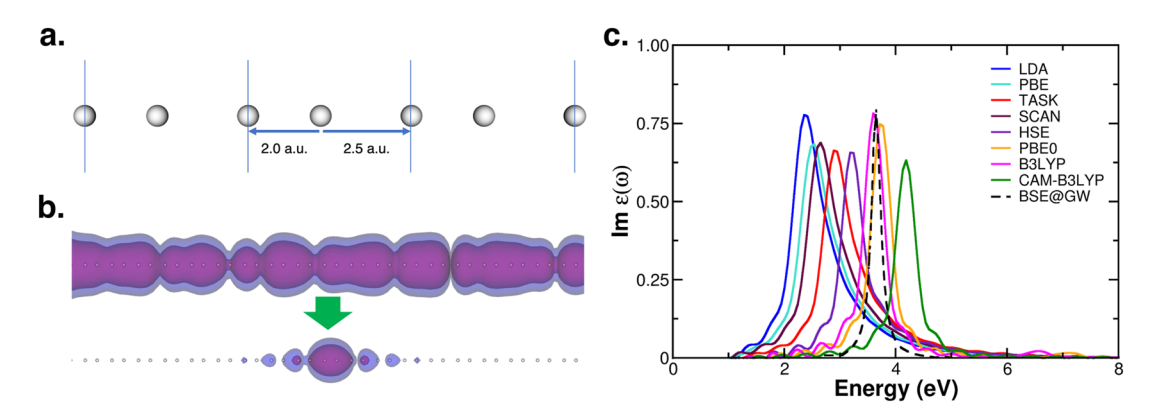


FIG. 3. (a) Geometry of the 2.0/2.5 a.u. spaced infinite hydrogen chain. Periodic boundaries are represented by blue lines. (b) A representative Bloch state and its corresponding TD-MLWF resulting from the unitary transformation. (c) Optical absorption spectra for the hydrogen chain obtained using a variety of XC approximations in RT-TDDFT. The BSE result, with GW quasiparticle energy shift, is shown in black for Ref. 94.

 $116~H_2$ units were found to give fully converged spectra with respect to chain length (see Fig. S4 in the supplementary material). All atoms were represented by HSCV norm-conserving pseudopotentials. 91

As shown in Fig. 3(b), the transformation of Bloch states to TD-MLWFs results in highly localized Wannier functions in space. For hybrid XC functionals, a cutoff distance (*R_{cutoff}*) of 30 bohrs was needed for obtaining a converged spectrum. This reduces the number of EXX integrals calculated to 11% and lowers the computational cost of hybrid XC functionals to ~5 times that of GGA (see Figs. S5 and S6 for details in the supplementary material). Additional information on parallelization and scaling is also included in the supplementary material (see Fig. S7). Figure 3(c) shows the resulting optical absorption spectra calculated for a variety of XC functionals of different sophistications, from LDA, GGA (PBE), and meta-GGAs (SCAN⁹⁶ and TASK⁷¹) to hybrids (PBE0, ⁸⁹ B3LYP, ⁹⁷ HSE, ⁹⁸ and CAM-B3LYP⁹⁹). The Bethe–Salpeter equation (BSE)^{100,101} result is also shown for comparison. Excitons are

described explicitly as particle-hole excitation in BSE via the two-particle Green's function, and the excitonic features are evident in the optical absorption spectrum of the H₂ chain. ⁹⁵ LDA, GGA, and meta-GGA functionals (LDA, PBE, SCAN, and TASK) yield absorption spectra that are much broader than the BSE spectrum and significantly red-shifted in energy. The hybrid XC functionals all offer improvements in terms of both peak position and shape. PBEO and B3LYP approximations perform similarly, yielding an energy difference of less than 0.1 eV compared to BSE. CAM-B3LYP, a popular range-corrected hybrid XC approximation for molecules, does not perform as well for this extended system, and the absorption peak is blue-shifted.

By changing the spacing to alternating distances of 2.0/2.05 a.u. between the hydrogen atoms in the chain [see Fig. 4(a)], the electronic properties of the chain become notably different. The exciton is more delocalized, 95 and we find less spatially localized Wannier functions when performing the MLWF transform [see Fig. 4(b)]. For

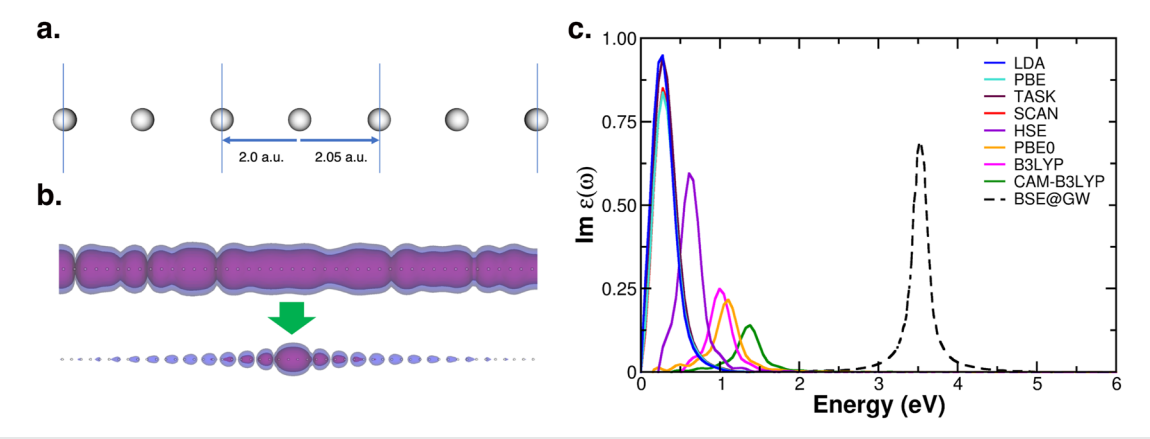


FIG. 4. (a) Geometry of the 2.0/2.05 a.u. spaced infinite hydrogen chain, with periodic boundaries represented by blue lines. (b) A representative Bloch state and its corresponding MLWF resulting from the unitary transformation. (c) Optical absorption spectra for the hydrogen chain obtained using a variety of XC approximations in RT-TDDFT. The BSE result, with GW quasiparticle energy shift, is shown in black for Refs. 102 and 103.

this 2.0/2.05 a.u. spaced chain, all simulation parameters were kept the same as the above 2.0/2.5 a.u. chain case, except for total simulation time, chain length, and simulation cell size. Here, a larger simulation cell containing 232 H₂ units (correspondingly, a 939.6 \times 20 \times 20 bohrs simulation cell) was needed for obtaining converged spectra (see Fig. S8 in the supplementary material for details). Additionally, simulations were run for 600 a.u. time following the delta kick. For this case, with more delocalized MLWFs, an R_{cutoff} of 100 bohrs was used, requiring 21% of the EXX integrals to be calculated. Despite the smaller savings we obtain, the cost of hybrid XC calculation is only 9 times that of PBE, compared to 23 times if all EXX pairs are needed (see Figs. S9 and S10 in the supplementary material for details). Figure 4(c) shows the calculated optical absorption spectrum using RT-TDDFT simulation with the same XC functionals as the 2.0/2.5 a.u. spaced hydrogen chain. While the hybrid XC functionals show improvement in terms of the peak position, all spectra show a peak significantly below the energy predicted by the BSE@GW calculation. Although these well-recognized hybrid XC approximations do not perform as well as one would hope, recent dielectric and other spatially dependent hybrid XC approximations for extended systems might fare better. The new hybrid XC implementation scheme based on the TD-MLWFs will allow RT-TDDFT simulations to benefit from new XC development.

III. OTHER RELATED DEVELOPMENTS

A. Anti-Hermitian correction of position operator in real-time dynamics

In the context of studying extended quantum systems, the question of how the quantum mechanical position operator $\hat{\bf r}$ should be defined is a longstanding challenge. Indeed, multiple formalisms have been proposed to address the definition of the position operator, as highlighted by previous studies in Refs. 104–106. In this work, we adopt Resta's definition structure theory community. Applying this formalism to the TD-KS framework, the Slater determinant consists of the TD-KS orbitals in the occupied/valence band manifold of N states, particularly when considering the Γ point approximation within the Brillouin Zone (BZ) sampling. Then, the time-dependent expectation value of the position operator at time t is given by

$$\langle \hat{\mathbf{r}}(t) \rangle = \frac{\mathbf{L}}{2\pi} \text{Im ln det}(\mathbf{S}(t)),$$
 (8)

where the $N \times N$ matrix **S** is

$$\mathbf{S}_{mn}(t) = \langle \psi_m(t) | e^{i\frac{2\pi}{\mathbf{L}}\hat{\mathbf{r}}} | \psi_n(t) \rangle. \tag{9}$$

This formulation is often known as the time-dependent Berry phase approach. In the real-time propagation of electron dynamics with an electric field applied through the length gauge, the position operator on a TD-KS state can be calculated by taking the functional derivative of Eq. (8) above, ¹⁰⁷

$$\hat{\mathbf{r}}|\psi_n(t)\rangle = \frac{\delta(\hat{\mathbf{r}}(t))}{\delta(\psi_n(t))} = \frac{\mathbf{L}}{2\pi} \text{Im} \sum_{m} e^{i\frac{2\pi}{\mathbf{L}}\hat{\mathbf{r}}|\psi_m(t)\rangle} \mathbf{S}_{mn}^{-1}(t), \quad (10)$$

where S_{mn}^{-1} represents the mnth element of the matrix inverse of S. By evolving the electron density using TD-MLWFs, denoted as $|w_n(t)\rangle$,

the above-mentioned formulation can be readily simplified to

$$\langle \hat{\mathbf{r}}(t) \rangle = \sum_{n} \mathbf{r}_{n}^{0}(t),$$
 (11)

where \mathbf{r}_n^0 is the position center (the expectation value for the position operator) for the *n*th TD-MLWF, defined as

$$\mathbf{r}_n^0(t) = \langle w_n(t) | e^{i\frac{2\pi}{L}\hat{\mathbf{r}}} | w_n(t) \rangle, \tag{12}$$

and Eq. (10) can be further transformed into

$$\hat{\mathbf{r}}|w_n(t)\rangle = \frac{\mathbf{L}}{2\pi} \operatorname{Im} \frac{e^{i\frac{2\pi}{\mathbf{L}}\hat{\mathbf{r}}}|w_n(t)\rangle}{\mathbf{r}_0^0(t)}.$$
 (13)

The definition of the position operator is solely provided through its expectation value, lacking an explicit formula for the operator itself. A direct consequence of the definition through the functional derivative is that the position operator may not inherently exhibit Hermitian properties. Anti-Hermitian characteristics might unphysically manifest into physical phenomena; the tunneling current across a thin insulating film is, for example, often non-zero although exponentially diminishing with film thickness, as discussed by Stengel and Spaldin. ¹⁰⁸ In RT-TDDFT simulations, this small but finite anti-Hermitian contribution can accumulate during the propagation, and the time-evolution operator could cease to be unitary. Consequently, the orthonormality of TD-KS orbitals can be disrupted during the propagation of real-time dynamics.

In order to illustrate how we can mitigate this potential problem, we consider the real-time dynamics of a polarized capacitor subjected to a perturbed electric field. In essence, the tunneling current component must be neglected by modifying the position operator such that Hermicity is restored. We introduce the Hermitian-corrected position operator as

$$\hat{\mathbf{r}}^{corr}|w_n(t)\rangle = \sum_m \frac{1}{2} |w_m(t)\rangle (\langle w_m|\hat{\mathbf{r}}|w_n\rangle + \langle w_n|\hat{\mathbf{r}}|w_m\rangle^*).$$
 (14)

To highlight the importance of the anti-correction scheme for the position operator, we present a simple example here. We consider the situation where a constant electric field, denoted as E(t)= E_0 , is applied to trans-polyacetylene along its chain direction. The strength of the electric field, E_0 , is chosen to be 0.0010 a.u., which is below the condition of dielectric breakdown.²⁵ Without employing the above-discussed correction to the position operator, the electronic energy of the system continuously increases erroneously, as shown in Fig. 5, while it should be constant.⁴⁷ With the corrected position operator, the simulation remains stable, and the energy remains constant despite small oscillatory behavior. We gain further insight by examining the TD-MLWF dynamics, as shown in Fig. 6. Although the displacements of the TD-MLWF centers do not show significant changes with or without the correction, the timedependent changes in their spreads are quite different. Without the correction, the averaged spread values continue to increase gradually with time without reaching a plateau until the simulation eventually crashes. This phenomenon can be attributed to the presence of an unphysical tunneling current, resulting in the accumulation of delocalization in the TD-MLWFs. Furthermore, due to the breakdown of unitarity, there is a continual loss of total electrons from the system. Therefore, in practical calculations, particularly for real-time

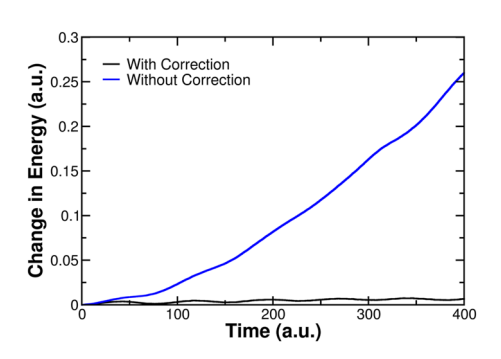


FIG. 5. Change in energy for trans-polyacetylene under a constant 0.0010 a.u. electric field with and without the anti-Hermitian correction applied.

simulations involving a continuous applied electric field, ^{12,25,26} it is essential to consider the anti-Hermitian correction to avoid these nonphysical features.

B. Refinement scheme with TD-MLWF

In traditional methods for computing polarization, such as the standard Berry-phase approach by King-Smith and Vanderbilt 109,110 and alternative formulas based on Wannier functions as proposed by Marzari and Vanderbilt, 85 a slow convergence, approximately $O(L^{-2})$, is observed with BZ sampling. 111 Here, L represents the linear dimension of the simulation cell (supercell) containing the isolated molecule or, alternatively, the resolution of the k-point mesh. 57 Consequently, for calculations with sparse BZ k-point grids, particularly when the Γ point approximation is employed, finite size

effects can introduce significant errors in the evaluation of polarization. To address this limitation in ground-state calculations, a "refinement" technique was introduced where minimal computational resources are needed. This refinement approach capitalizes on the existence of a well-localized set of MLWFs, and the convergence of simulation supercell size or, equivalently, BZ k-point sampling, can be drastically improved in the polarization calculations of the ground state. Here, we extend this formalism to real-time dynamics using the TD-MLWFs. We begin this extension by evaluating the expectation value of a local operator $V(\mathbf{r})$ for each Wannier function w_n in real space

$$\langle w_n | V | w_n \rangle = \int_{p^3} |w_n(\mathbf{r})|^2 V(\mathbf{r}) d\mathbf{r},$$
 (15)

equivalently in the momentum *q*-space, we have

$$\langle w_n | V | w_n \rangle = \int_{|q| < E_{cut}} \widetilde{V}^*(\mathbf{q}) \widetilde{\rho}_n(\mathbf{q}) d\mathbf{q},$$
 (16)

where $\widetilde{\rho}_n(\mathbf{q})$ is the continuous Fourier transformation of the Wannier density $\rho_n(\mathbf{r}) = |w_n(\mathbf{r})|^2$. When working with localized Wannier functions that have negligible values beyond a specific distance from their centers, it becomes possible to confine the corresponding integrals to a well-defined spatial region. This region can take the form of a cubic box centered around the region where the Wannier density is non-zero. Therefore, the q-space integral in Eq. (16) can be transformed into a summation over a distinct set of reciprocal space vectors, which remain finite due to the plane-wave cutoff, E_{cut} . If this integration box is smaller than the region where the Wannier density is non-zero, an error arises from the reciprocal-space summation. This error is due to the overlap of the tails of Wannier functions

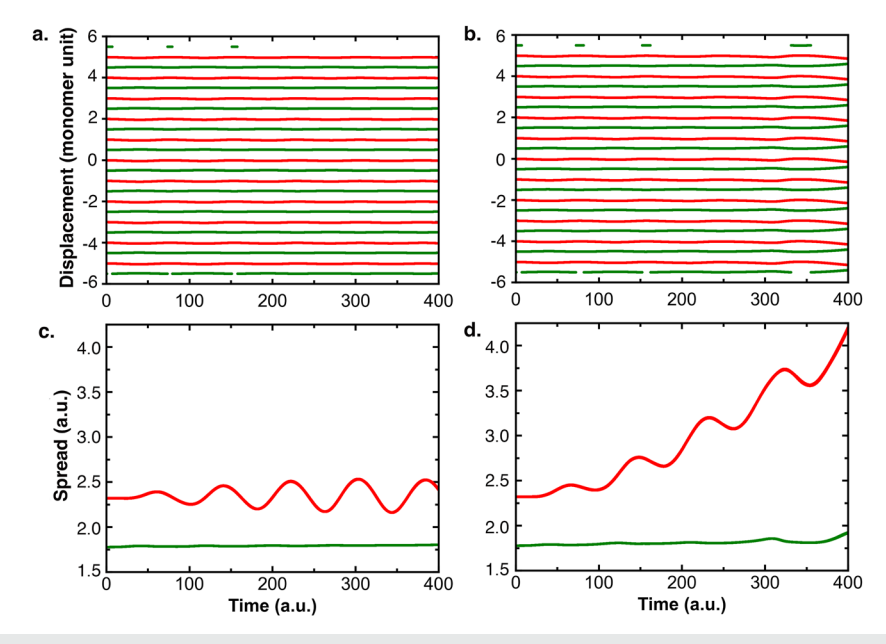


FIG. 6. Displacement of the C–C double bond Wannier centers (red) and C–C single bond Wannier centers (green) (a) with the anti-Hermitian correction and (b) without the correction. Average spread of the C–C double bond Wannier centers (red) and C–C single bond Wannier centers (green) (c) with the anti-Hermitian correction and (d) without the correction.

and their artificially duplicated images. The magnitude of this overlap depends on the localization properties of the Wannier state and, specifically, diminishes exponentially to zero when $w_n(\mathbf{r})$ exhibits exponential localization. The refinement scheme is reliant on the exponential decay characteristics of the Wannier functions. By performing q-space integrals across the Born-von-Kármán (BvK) cell and assuming exponential decay for the Wannier functions, we can achieve exponential convergence in the calculated expectation values for any operator. Ideally, the integration domain in real space should correspond to a Wigner–Seitz BvK cell centered around the Wannier function. We can then define a correction operator for local operator $V(\mathbf{r})$ as

$$\widetilde{V}(\mathbf{b}) = \frac{1}{V_{BvK}} \int_{Wigner-Seitz} e^{-i\mathbf{b}\mathbf{r}} V(\mathbf{r}) d\mathbf{r}.$$
 (17)

Subsequently, the expectation value is merely expressed as

$$\langle w_n | V | w_n \rangle = V_{BvK} \sum_{\mathbf{b}} \widetilde{V}^*(\mathbf{b}) \widetilde{\rho}(\mathbf{b}).$$
 (18)

For the refinement of the position operator of a supercell calculation at the Γ point, we seek the refined expectation value of the position as

$$\langle \mathbf{r}_n \rangle = \langle \mathbf{r}_n^0 \rangle + \Delta \mathbf{r}_n.$$
 (19)

Here, \mathbf{r}_n^0 is specified by Eq. (10) and $\Delta \mathbf{r}_n$ is the refinement we seek to compute. The ν th Cartesian component of $\Delta \mathbf{r}_n$, denoted as $\Delta r_{n,\nu}$, can be computed in real space using a periodic saw-tooth function $X_{n,\nu}(r_{\nu})$ centered at the MLWF center \mathbf{r}_n^0 .

Then, the refined position operator can be expressed as

$$\Delta r_{n,\nu} = \langle w_n | u_{n,\nu} \rangle,\tag{20}$$

where $u_{n,\nu}(r) := X_{n,\nu}(r_{\nu})w_n(r)$. Given that the TD-MLWFs exhibit exponential decay in real space, the discontinuity of the saw-tooth

function does not substantially influence the numerical stability of the refinement process. ¹⁰⁷ The refinement scheme also contributes when applying a length-gauge external electric field in RT-TDDFT propagation, as the refined position operator can be defined as

$$\hat{r}_{v}^{ref}|w_{n}(t)\rangle = \hat{r}_{v}^{0}|w_{n}(t)\rangle + |u_{n,v}(t)\rangle, \tag{21}$$

$$X_{n,\nu}(r_{\nu}) = \begin{cases} r_{\nu} - r_{n,\nu}^{0} + L_{\nu} & \text{if } r_{\nu} - r_{n,\nu}^{0} \le -L_{\nu}/2, \\ r_{\nu} - r_{n,\nu}^{0} & \text{if } r_{\nu} - r_{n,\nu}^{0} \in (-L_{\nu}/2, L_{\nu}/2), \\ r_{\nu} - r_{n,\nu}^{0} - L_{\nu} & \text{if } r_{\nu} - r_{n,\nu}^{0} \ge L_{\nu}/2. \end{cases}$$
(22)

To demonstrate the utility of this refinement approach, particularly with an applied electric field, computation of the optical absorption spectrum of crystalline silicon using RT-TDDFT simulation is considered. A delta kick in the form of an impulsive electric field was applied for a time duration of 0.05 a.u. The electric field was subsequently turned off, and the system was propagated for an additional 250 a.u. time in the MLWF gauge using the (ETRS)⁹⁰ propagator and a 0.05 a.u. time step. A kinetic energy cutoff of 40 Ry was used for plane-wave expansion of the TD-KS orbitals. Even using an unsatisfactorily small 8-atom (32 electron) supercell, the refinement approach can improve the spectrum, reducing noise above 4 eV and enhancing the higher energy peak, as shown in Fig. 7(a). Using the more reasonable 128-atom (512 electron) supercell, which is elongated in the x-direction by repeating the 8-atom cell 16 times, the refinement approach shows improvement even though it is not as significant [Fig. 7(b)]. Importantly, this absorption spectrum agrees almost identically with the result using a larger 256-atom supercell (1024 electron) elongated in the x-direction. In essence, the refinement method allows us to employ a smaller supercell than normally possible to obtain a converged result for extended systems, 12 yielding significant savings in the computational

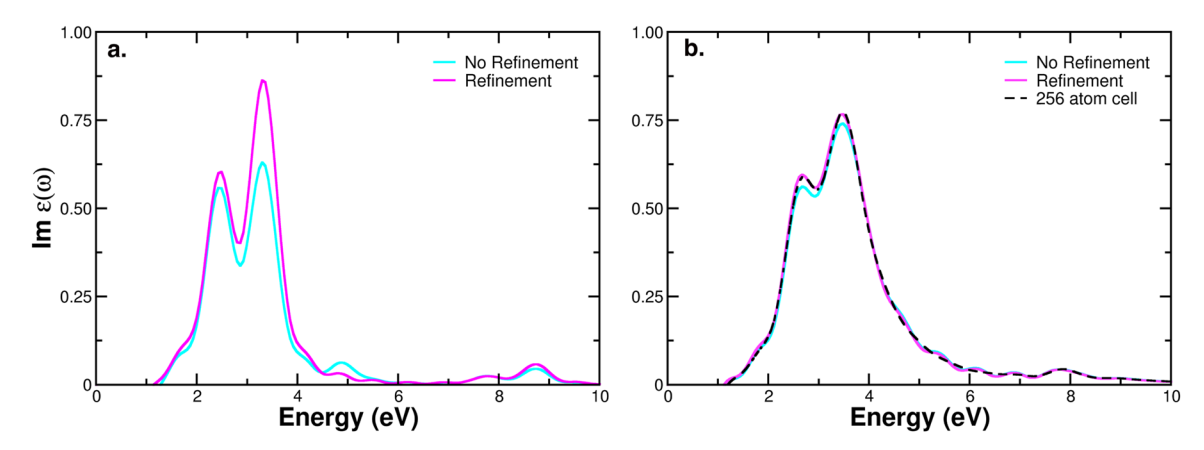


FIG. 7. Optical absorption spectrum for (a) an 8-atom silicon cell and (b) an 128-atom silicon cell with and without refinement for the TD-MLWFs. Although a larger improvement is observed for the smaller silicon cell, the refined result for the 128-atom cell gives an identical result to that of a 256-atom cell (dashed black line).

C. Length vs velocity gauge for extended systems

RT-TDDFT allows us to model the dynamic response of electrons to classical electromagnetic fields, with applications ranging from optical excitation 112-114 to plasmonics 11 magnetic circular dichroism. 10,117,118 The electric field is typically incorporated into the Hamiltonian using the long-wavelength approximation. 23,119,120 Despite the formal limitation regarding the homogeneous field applied to extended systems in the Runge-Gross theorem, requiring time-dependent current density functional theory (TDCDFT), 121 empirical observations indicate that many response properties can be accurately acquired within the framework of TDDFT using RT-TDDFT simulation. 12,29 Beyond this formal theoretical issue for applying the electric field, the PW-PP implementation of TDDFT faces another practical question. When the potential in the Hamiltonian [Eq. (2)] is local, the electric field exhibits gauge invariance such that it can be represented through the scalar potential or the vector potential in the Hamiltonian, namely the length gauge or the velocity gauge. However, as Starace and others 122-124 have noted, when a non-local potential is present within the Hamiltonian, the gauge invariance is no longer preserved. In the PW-PP implementation, non-local pseudopotentials are utilized to model core electrons, and strictly speaking, the length and velocity gauges are no longer equivalent. Although previous studies on isolated systems have addressed this issue^{23,125} and demonstrated that both gauges yield equivalent results, it has remained a persistent problem for the optical properties of extended systems. In the more-widely used length gauge, the electric field is represented as an additional scalar potential in the KS Hamiltonian [Eq. (2)],

$$\hat{v}_E(t) = e\mathbf{E}(t)\hat{\mathbf{r}},\tag{23}$$

where $\mathbf{E}(t)$ is the time-dependent electric field and $\hat{\mathbf{r}}$ is the position operator. Then, the TD-KS equation becomes

$$i\frac{d}{dt}|\psi_{n}(\mathbf{r},t)\rangle = \left\{-\frac{1}{2}\nabla_{\mathbf{r}}^{2} + \hat{v}_{ext}(\mathbf{r},t) + \int d\mathbf{r}' \frac{\rho(\mathbf{r}',t)}{|\mathbf{r}-\mathbf{r}'|} + \hat{v}_{XC}(\mathbf{r},t) + e\mathbf{E}(t)\hat{\mathbf{r}}\right\}|\psi_{n}(\mathbf{r},t)\rangle. \tag{24}$$

The choice of $\hat{v}_E(t)$ here is not unique, however. Through the gauge invariance principle of electrodynamics, the physical properties of the system do not change even if it is subjected to another scalar potential

$$\hat{v}_E'(t) = \hat{v}_E(t) + \frac{d}{dt}\chi(\mathbf{r}, t). \tag{25}$$

Here, $\chi(t)$ defines the gauge transform from the length gauge to the velocity gauge

$$\chi(\mathbf{r},t) = -\mathbf{r} \cdot \mathbf{A}(t), \tag{26}$$

where $\mathbf{A}(t)$ is the corresponding magnetic field given by the vector potential

$$\mathbf{A}(t) = -c \int_{-\infty}^{t} \mathbf{E}(t') dt'. \tag{27}$$

With the transformation in Eq. (25), the KS orbitals change as

$$\psi_n(\mathbf{r},t) \to \psi'_n(\mathbf{r},t) = e^{i\chi(\mathbf{r},t)}\psi_n(\mathbf{r},t),$$
 (28)

where the prime corresponds to the gauge-transformed orbitals. If the potential is strictly local in the Hamiltonian, the resulting TD-KS equation in the so-called velocity gauge can be expressed as

$$i\frac{d}{dt}|\psi'_{n}(\mathbf{r},t)\rangle = \left\{\frac{1}{2}\left(-i\nabla_{\mathbf{r}} + \frac{e}{c}\mathbf{A}(t)\right)^{2} + \hat{v}_{ext}(\mathbf{r},t)\right.$$
$$+ \int d\mathbf{r}' \frac{\rho(\mathbf{r}',t)}{|\mathbf{r}-\mathbf{r}'|} + \hat{v}_{XC}(\mathbf{r},t)\right\}|\psi'_{n}(\mathbf{r},t)\rangle. \tag{29}$$

Both Eqs. (24) and (29) yield the same set of physical observables, 23,122,124 and the transformation is gauge invariant for a local potential. However, as noted earlier, the PW-PP implementation uses non-local pseudopotentials, which makes v_{ext} non-local. Note that the XC potential could also be non-local for certain types of XC approximations, such as hybrids. In practice, the external potential in the PW-PP implementation is expressed as the sum of local and non-local (nl) potentials,

$$\hat{v}_{ext}(\mathbf{r},t) = \hat{v}_{ext}^{local}(\mathbf{r},t) + \hat{v}_{ext}^{nl}(t). \tag{30}$$

With the gauge specified by Eq. (26), the non-local part of the potential transforms as

$$\hat{v}_{ext}^{nl}(t) \rightarrow \hat{v}_{ext}^{nl}(t)' = e^{i\chi(\mathbf{r},t)} \hat{v}_{ext}^{nl}(t) e^{-i\chi(\mathbf{r},t)}
= e^{-i\mathbf{r}\cdot\mathbf{A}(t)} \hat{v}_{ext}^{nl}(t) e^{i\mathbf{r}\cdot\mathbf{A}(t)},$$
(31)

making the non-local potential gauge dependent, as it contains the vector potential. In practical calculations, an approximate form is often used. ^{126,127} For extended periodic systems, the velocity-gauge is widely used in TDDFT^{29,114,128} because delocalized KS orbitals complicate the use of the length gauge with the periodic boundary conditions. However, with TD-MLWFs and the position operator defined as Eq. (7), the same electric field can be applied to individual TD-MLWFs¹²⁹ as described in our previous work. ¹² Alternatively, the same electric field can be applied using the velocity gauge via the vector potential, as typically performed for extended systems. ⁹⁴

We here examine the extent to which the difference between using the length and velocity gauges manifests in PW-PP based RT-TDDFT simulations by calculating optical absorption spectra. We again turn to the one-dimensional hydrogen chain, specifically the optical excitation of the 2.0/2.5 a.u. spaced chain [see Fig. 3(a)]. For the length gauge, we followed the procedure detailed in Sec. II B to determine the optical absorption. For the velocity gauge, the same simulation cell was used, containing 116 H₂ units along with the HSCV pseudopotential for hydrogen. A delta kick was applied through a step function in the vector potential

$$\mathbf{A}(t) = \begin{cases} 0 \text{ a.u.} & t < 0 \text{ a.u.,} \\ 0.001 \text{ a.u.} & t \ge 0 \text{ a.u.,} \end{cases}$$
 (32)

with the magnitude chosen to match that of the length gauge electric field pulse. The TD-KS wavefunctions were propagated for 400 a.u. time using the ETRS propagator 90 and a 0.05 a.u. time step. From the simulation, we obtain the macroscopic current

$$\mathbf{J}(t) = \frac{1}{2} \int d\mathbf{r} \sum_{n} f_{n} \psi_{n}^{*}(\mathbf{r}, t) \nabla \psi_{n}(\mathbf{r}, t) + \text{c.c.},$$
 (33)

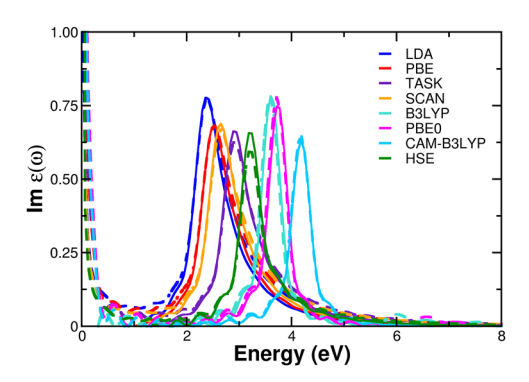


FIG. 8. Optical absorption spectra for the 2.0/2.5 a.u. spaced hydrogen chain using the velocity gauge (dashed lines) and length gauge (solid lines) for a variety of XC functionals

where f_n is the occupation of the TD-KS wavefunctions, and the current is used to calculate the dielectric function using the same prescription as detailed in Ref. 12. The same damping function, as used with the length gauge and described in Sec. II B, was used. Figure 8 shows the resulting absorption spectra from the length gauge (LG) (solid lines) and velocity gauge (VG) (dashed lines) for a variety of XC functionals. The peak positions are identical for both gauges. Interestingly, we observe what is commonly identified as an artificial peak, or "fake plasmon," around 0 eV for the velocity gauge 58,130,131 for all functionals except the hybrid B3LYP functional. Note that this artificial peak can be removed by subtracting the background current, as detailed in Ref. 113, or by using a very dense k-grid, as detailed in Ref. 130. We include this peak to highlight its presence when studying extended systems utilizing the velocity gauge and how the peak vanishes when moving to the B3LYP functional. Additionally, the agreement for the hybrid XC functionals (B3LYP, PBE0, and CAM-B3LYP) is notable here, as hybrid XC approximations introduce an additional non-local potential in the KS Hamiltonian. To confirm the generality of the gauge equivalence, we compared the optical spectra of the 2.0/2.05 a.u. spaced hydrogen chain using both the length and velocity gauges. As expected, the peak positions were identical (see Fig. S11 in the supplementary material for details). The potential effect of gauge invariance arises directly from the use of non-local pseudopotentials and not from the system being studied. Therefore, while the conclusion could be affected if the pseudopotentials are not constructed properly, it should remain consistent across different systems otherwise. Therefore, despite formal and practical complications, both gauges can be used to reliably acquire key response properties of extended systems.

D. Modeling isolated systems using the PW-PP formalism

While the PW-PP formulation is highly efficient and widely used when studying extended periodic systems, certain care must be taken when it is applied to isolated systems, especially for the calculation of excited-state properties. A simulation cell of a $15 \times 15 \times 15$ bohrs³ is large enough to minimize interactions with its periodic images, for instance, when calculating most ground-state properties

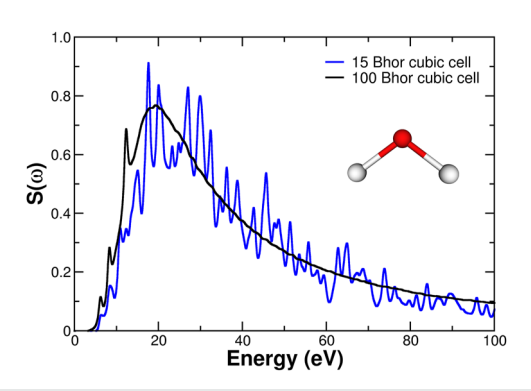


FIG. 9. Dipole strength function (absorption spectrum) of gas-phase water, using the LDA XC functional and a 40 Ry cutoff energy, at different cell sizes.

of gas-phase water. However, when modeling properties involving electronic excitation, such as optical absorption spectra, interactions with periodic images in RT-TDDFT simulation can lead to significant errors, as shown in Fig. 9. An enormous simulation cell, as large as $100 \times 100 \times 100$ bohrs³, is needed to obtain the fully converged optical spectra.¹² This significantly increases the number of basis set functions from 57 657 plane-waves for the (15 bohrs)³ cell to 17 088 048 plane-waves for the (100 bohrs)³ cell needed for a kinetic energy cutoff of 40 Ry. RT-TDDFT PW-based codes scale at a rate of $O(N_n N_{pw} \log N_{pw})$, where N_n is the number of Kohn–Sham states and N_{pw} is the number of plane-waves in the basis set. Therefore, the use of a (100 bohrs)³ cubic cell makes the calculation ~450× more expensive. For optical absorption spectra calculations, which typically require a minimum of a few femto-seconds (fs) to converge, the increased computational cost can quickly become untenable. By eliminating spurious interactions of the isolated system with its periodic images, the cell size needed for RT-TDDFT calculations (and, in turn, the computational cost) can be significantly reduced.

One cause of the spurious interactions arises from long-range electrostatic interactions between neighboring periodic cells. We first examine the Martyna–Tuckerman (MT) approach¹³² to remove these types of interactions, the basic idea being simply to modify the Hartree potential such that it is still periodic but free from contributions from neighboring cells.¹³³ The Hartree potential is expressed in real space using Green's function as

$$v_H(\mathbf{r}) = \int d\mathbf{r}' \rho(\mathbf{r}', t) G(\mathbf{r} - \mathbf{r}'), \tag{34}$$

where Green's function for isolated systems is given by

$$G(\mathbf{r} - \mathbf{r'}) = \frac{1}{|\mathbf{r} - \mathbf{r'}|}.$$
 (35)

In practical PW-PP based calculations, the Hartree potential in the periodic simulation cell is evaluated in the reciprocal space using a discrete set of wave vectors, **g**, to expand the function. However, in practice, the calculation of the Fourier transform (FT) of Eq. (35)

results in unavoidable periodic interactions. The Fourier transform of Eq. (35) is calculated as

$$\widetilde{G}(\mathbf{g}) = \int_{\infty} G(\mathbf{r}) e^{-i\mathbf{g}\cdot\mathbf{r}} d\mathbf{r} = \int_{\Omega} \sum_{R} G(\mathbf{r} + \mathbf{R}) e^{-i\mathbf{g}\cdot\mathbf{r}} d\mathbf{r}$$

$$= \int_{\Omega} G_{p}(\mathbf{r}) e^{-i\mathbf{g}\cdot\mathbf{r}} d\mathbf{r}, \qquad (36)$$

where $G_p(\mathbf{r})$ is the periodic Green's function in real space and Ω is the periodic simulation cell volume.¹³⁴ This Fourier transform of Green's function unavoidably includes interactions from periodic images. Instead of $G_p(\mathbf{r})$, we wish to build the Green's function as

$$G(\mathbf{r}) = \sum_{\mathbf{g}} G(\mathbf{g}) e^{-i\mathbf{g} \cdot \mathbf{r}}, \tag{37}$$

where $G(\mathbf{g})$ are the Fourier series coefficients of the true non-periodic Hartree potential. We express the Fourier series coefficients as the sum of the Fourier transform of Green's function, $\widetilde{G}(\mathbf{g})$, with an auxiliary function to correct the FT for the incorrect interactions with periodic images,

$$G(\mathbf{g}) = \widetilde{G}(\mathbf{g}) + \Delta G(\mathbf{g}), \tag{38}$$

where $\Delta G(\mathbf{g})$ is the auxiliary function correction. Assuming that the simulation cell is large enough so that the Fourier transform of short-range potentials is correct, only long-range corrections need to be determined. For our work, this amounts to correcting the long-range Coulomb and pseudopotential terms as described by Hine *et al.*¹³³ In terms of the corresponding Hartree potential, we have

$$v_H(\mathbf{r}) = \sum_{\mathbf{g}} \frac{4\pi}{\Omega} \rho(\mathbf{g}, t) \left(\frac{1 - \delta_{\mathbf{g}, 0}}{g^2} + \Delta G(\mathbf{g}) \right) e^{i\mathbf{g} \cdot \mathbf{r}}, \tag{39}$$

with

$$\Delta G(\mathbf{0}) = \lim_{\mathbf{g} \to \mathbf{0}} \left(\tilde{G}(\mathbf{g}) - \frac{1}{g^2} \right), \tag{40}$$

and

$$\Delta G(\mathbf{g}) = \int_{\Omega} e^{-i\mathbf{g}\cdot\mathbf{r}} \frac{\operatorname{erf}(\alpha r)}{r} d\mathbf{r},$$
(41)

where α is the parameter that determines the short to long range transition point, such that the correct behavior of the Green's function for isolated systems [Eq. (35)] is restored in the reciprocal space. ¹³⁴

Figure 10 shows the effect of the MT correction in the RT-TDDFT simulation for calculating the optical absorption spectra of a gas-phase water molecule. A small but noticeable improvement is observed for the (15 bohrs)³ simulation cell, as shown in Fig. 10(a). Using a slightly larger simulation cell, the spectra with and without the MT corrected potential are now identical, as seen in Fig. 10(b). However, the unphysical "wiggles" are still present in the absorption spectrum. These results indicate that long-range electrostatic interaction is not the major source of error.

Another possible source of error in the calculation of optical absorption spectra is ionized electrons reaching the simulation cell boundaries. Even though it may not be large, a finite (non-zero) probability density reaches the boundaries during the RT-TDDFT simulation, and this density could interact with the periodic images. One practical approach to mitigate this problem is to set up a spatial region near the boundaries of the simulation cell such that the electron density is effectively removed from the simulation. ^{135,136} Here, we examine the idea of using a complex absorbing potential (CAP) by modifying the Hamiltonian [Eq. (2)] such that a complex (imaginary) potential at the boundaries of the simulation cell absorbs any finite probability density. ^{112,137,138} This approach has been previously used successfully in RT-TDDFT simulation with a real-space grid basis for investigating the optical absorption spectra

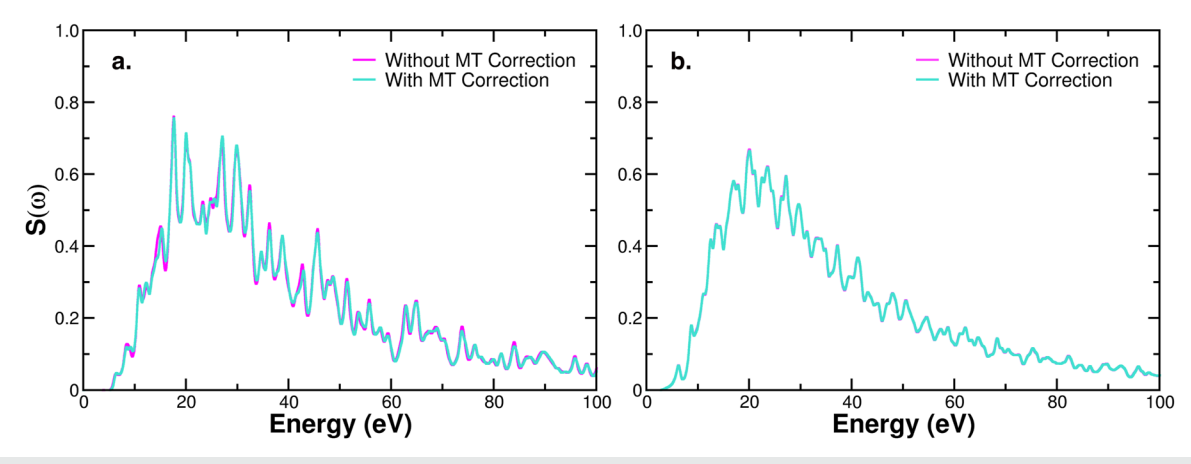


FIG. 10. Dipole strength function (absorption spectrum) with (cyan) and without (magenta) the MT correction for gas-phase water in (a) 15 bohrs cubic cell and (b) 25 bohrs cubic cell. All simulations are performed using the LDA functional and a cutoff energy of 40 Ry.

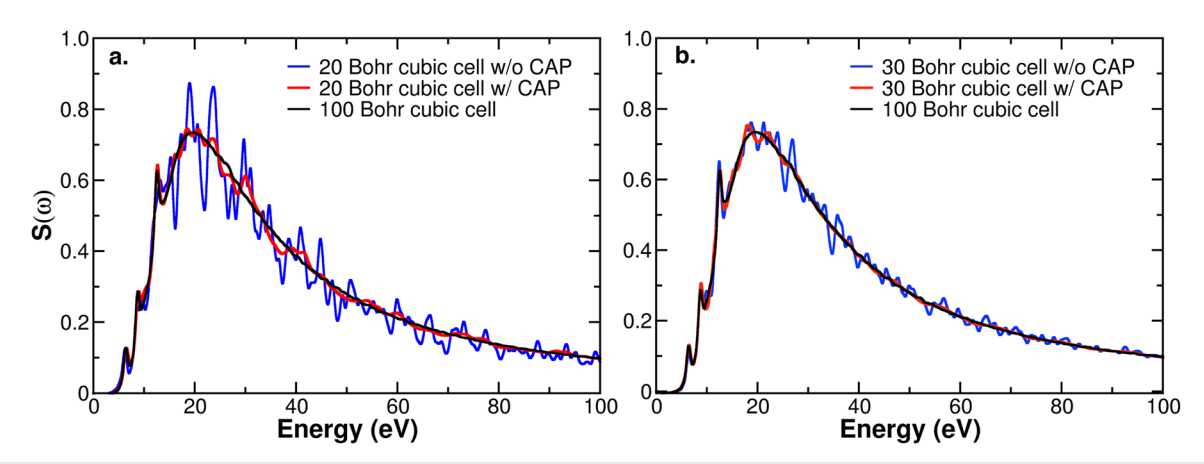


FIG. 11. Dipole strength function (absorption spectra) with (red) and without (blue) a complex absorbing potential (CAP) for gas-phase water in a (a) 20 bohrs cubic cell and a (b) 30 bohrs cubic cell. The absorption spectrum for a 100 bohrs cubic cell is shown in black for comparison. All simulations are performed using the LDA functional and a cutoff energy of 40 Ry.

of molecules¹¹² and the photo-emission spectra of 2D materials.¹³⁹ We extend the idea to the PW-PP formalism and employ a CAP of the following form:

$$v_{abs}(\mathbf{r}, t > 0) = -iW(\mathbf{r}) = \begin{cases} 0 & (0 < \mathbf{r} < \mathbf{R}), \\ -iW_0 \frac{\mathbf{r} - \mathbf{R}}{\Delta \mathbf{R}} & (\mathbf{R} < \mathbf{r} < \mathbf{R} + \Delta \mathbf{R}), \end{cases}$$
(42)

where W_0 is the maximum of the chosen potential, **R** is the position of the front boundary (starting point) of the CAP, and $\Delta \mathbf{R}$ is the width of the CAP. For gas-phase water, we tested a 20 bohrs cubic simulation cell with a CAP of $W_0 = 1.2$ a.u., $\mathbf{R} = 9.0$ a.u., and Δ **R** = 14.0 a.u., and a 30 bohrs cubic simulation cell with a CAP of $W_0 = 1.2 \text{ a.u.}, \mathbf{R} = 12.0 \text{ a.u.}, \text{ and } \Delta \mathbf{R} = 20.0 \text{ a.u.}$ As shown in Fig. 11(a), for the 20 bohrs cell, the CAP significantly reduces wiggles in the spectra, and the result is in close agreement with that of the fully converged 100 bohrs cell. For the larger 30 bohrs cell [Fig. 11(b)], using the CAP results in a nearly identical spectra to that of the 100 bohrs cell. Compared to the 17 088 048 plane-waves required for simulating a water molecule in the 100 bohrs cell, only 461 165 plane-waves are needed for the 30 bohrs cell, and the CAP does not incur any additional computational cost. The computational cost of the 30 bohrs cell is thus lowered to only 9.5× more expensive than that of the 15 bohrs cell, significantly less than the cost of the 100 bohrs cell (450× more expensive). While care should be taken in determining the parameters of the absorbing potential to prevent reflection, 137 its usage can significantly reduce the cost of modeling isolated systems using RT-TDDFT simulation based on the PW-PP formalism.

IV. CONCLUSION

In this work, we provide and document several recent developments of RT-TDDFT in the PW-PP formalism. In addition to demonstrating the reduction in the computational cost of the exact

exchange calculation when using time-dependent maximally localized Wannier functions (TD-MLWFs), we discuss several related developments that are useful for the community. Additional developments include the anti-Hermitian correction for TD-MLWFs when a continuous electric field is applied through the length gauge, the refinement procedure for the TD-MLWFs, the assessment of the velocity and length gauge approaches for applying an electric field, and the usage of a complex absorbing potential (CAP), as well as the periodic image correction when modeling isolated systems in the PW-PP formalism. All the developments discussed in this work are available as open-source code under a new forked version, Qb@ch. ⁵⁹

SUPPLEMENTARY MATERIAL

See the supplementary material for calculation of isolated systems using EXX, details on the convergence of the silicon cell with respect to cell size and cutoff energy, determination of the cell size and the R_{cutoff} needed for the hydrogen chains, the computational cost of different XC functionals for the hydrogen chains, scaling for the 2.0/2.5 a.u. spaced chain when using hybrid functionals, and additional comparisons between the length and velocity gauges.

ACKNOWLEDGMENTS

This work was partially supported by the National Science Foundation under Award Nos. CHE-1954894 and OAC-2209858 for the development of RT-TDDFT methodologies. We acknowledge the Research Computing at the University of North Carolina at Chapel Hill for computer resources. An award of computer time was also provided by the Innovative and Novel Computational Impact on Theory and Experiment (INCITE) program. This research used resources from the Argonne Leadership Computing Facility (ALCF), which is a DOE Office of Science User Facility supported under Contract No. DE-AC02-06CH11357.

AUTHOR DECLARATIONS

Conflict of Interest

The authors have no conflicts to disclose.

Author Contributions

C.S. and R.Z. led and contributed equally to the work. All authors discussed the results and contributed to the final article.

Christopher Shepard: Conceptualization (equal); Data curation (equal); Formal analysis (equal); Investigation (equal); Methodology (equal); Writing – original draft (equal); Writing – review & editing (equal). Ruiyi Zhou: Conceptualization (equal); Data curation (equal); Formal analysis (equal); Investigation (equal); Methodology (equal); Writing – original draft (equal); Writing – review & editing (equal). John Bost: Formal analysis (equal); Writing – review & editing (equal). Tom Carney: Formal analysis (equal); Writing – review & editing (equal). Yi Yao: Conceptualization (equal); Formal analysis (equal); Investigation (equal); Methodology (equal); Writing – review & editing (equal). Yosuke Kanai: Conceptualization (equal); Formal analysis (equal); Funding acquisition (equal); Methodology (equal); Project administration (equal); Writing – review & editing (equal).

DATA AVAILABILITY

The data that support the findings of this study are available from the corresponding author upon reasonable request. The code used in the current study is available on GitHub (https://github.com/chrsshpr/QBACH).

REFERENCES

- ¹ K. Yabana and G. F. Bertsch, Phys. Rev. B 54, 4484 (1996).
- ²X. Li, N. Govind, C. Isborn, A. E. I. DePrince, and K. Lopata, Chem. Rev. 120, 9951 (2020).
- ³K. Yabana and G. Bertsch, Int. J. Quantum Chem. **75**, 55 (1999).
- ⁴C. Shepard, R. Zhou, D. C. Yost, Y. Yao, and Y. Kanai, J. Chem. Phys. **155**, 100901 (2021)
- ⁵J. Xu, T. E. Carney, R. Zhou, C. Shepard, and Y. Kanai, J. Am. Chem. Soc. **146**, 5011 (2024).
- ⁶M. E. Casida, "Time-dependent density functional response theory for molecules," in *Recent Advances in Density Functional Methods*, edited by D. P. Chong (World Scientific, Singapore, 1995), Vol. 1, pp. 155–192.
- ⁷M. E. Casida and M. Huix-Rotllant, Annu. Rev. Phys. Chem. **63**, 287 (2012).
- ⁸K. Burke, J. Werschnik, and E. K. U. Gross, J. Chem. Phys. **123**, 62206 (2005).
- ⁹E. Runge and E. K. U. Gross, Phys. Rev. Lett. **52**, 997 (1984).
- ¹⁰ J. J. Goings and X. Li, J. Chem. Phys. **144**, 234102 (2016).
- ¹¹ R. G. Fernando, M. C. Balhoff, and K. Lopata, J. Chem. Theory Comput. 11, 646 (2015).
- ¹²D. C. Yost, Y. Yao, and Y. Kanai, J. Chem. Phys. 150, 194113 (2019).
- ¹³W.-H. Liu, Z. Wang, Z.-H. Chen, J.-W. Luo, S.-S. Li, and L.-W. Wang, Wiley Interdiscip. Rev.: Comput. Mol. Sci. 12, e1577 (2022).
- ¹⁴S. Tussupbayev, N. Govind, K. Lopata, and C. J. Cramer, J. Chem. Theory Comput. 11, 1102 (2015).
- ¹⁵K. Lopata, B. E. Van Kuiken, M. Khalil, and N. Govind, J. Chem. Theory Comput. 8, 3284 (2012).
- ¹⁶C. Shepard, D. C. Yost, and Y. Kanai, Phys. Rev. Lett. 130, 118401 (2023).
- ¹⁷C. Shepard and Y. Kanai, J. Phys. Chem. B **127**, 10700 (2023).
- ¹⁸D. C. Yost, Y. Yao, and Y. Kanai, J. Phys. Chem. Lett. 11, 229 (2020).

- ¹⁹ J. M. Pruneda, D. Sánchez-Portal, A. Arnau, J. I. Juaristi, and E. Artacho, Phys. Rev. Lett. 99, 235501 (2007).
- ²⁰ A. Schleife, Y. Kanai, and A. A. Correa, Phys. Rev. B **91**, 014306 (2015).
- ²¹ Y. Yao, D. C. Yost, and Y. Kanai, Phys. Rev. Lett. 123, 066401 (2019).
- ²²D. C. Yost and Y. Kanai, J. Am. Chem. Soc. **141**, 5241 (2019).
- ²³ J. Mattiat and S. Luber, J. Chem. Theory Comput. **18**, 5513 (2022).
- ²⁴H. Hübener, M. A. Sentef, U. De Giovannini, A. F. Kemper, and A. Rubio, Nat. Commun. 8, 13940 (2017).
- ²⁵R. Zhou, D. C. Yost, and Y. Kanai, J. Phys. Chem. Lett. **12**, 4496 (2021).
- ²⁶R. Zhou and Y. Kanai, J. Phys. Chem. Lett. **14**, 8205 (2023).
- ²⁷M. S. Mrudul, N. Tancogne-Dejean, A. Rubio, and G. Dixit, npj Comput. Mater. **6**, 10 (2020).
- ²⁸ N. Tancogne-Dejean, O. D. Mücke, F. X. Kärtner, and A. Rubio, Phys. Rev. Lett. 118, 087403 (2017).
- ²⁹ M. Noda, S. A. Sato, Y. Hirokawa, M. Uemoto, T. Takeuchi, S. Yamada, A. Yamada, Y. Shinohara, M. Yamaguchi, K. Iida, I. Floss, T. Otobe, K.-M. Lee, K. Ishimura, T. Boku, G. F. Bertsch, K. Nobusada, and K. Yabana, Comput. Phys. Commun. 235, 356 (2019).
- ³⁰ J. M. Soler, E. Artacho, J. D. Gale, A. García, J. Junquera, P. Ordejón, and D. Sánchez-Portal, J. Phys.: Condens. Matter 14, 2745 (2002).
- ³¹ Y. Takimoto, F. D. Vila, and J. J. Rehr, J. Chem. Phys. 127, 154114 (2007).
- ³²T. D. Kühne, M. Iannuzzi, M. Del Ben, V. V. Rybkin, P. Seewald, F. Stein, T. Laino, R. Z. Khaliullin, O. Schütt, F. Schiffmann, D. Golze, J. Wilhelm, S. Chulkov, M. H. Bani-Hashemian, V. Weber, U. Borštnik, M. Taillefumier, A. S. Jakobovits, A. Lazzaro, H. Pabst, T. Müller, R. Schade, M. Guidon, S. Andermatt, N. Holmberg, G. K. Schenter, A. Hehn, A. Bussy, F. Belleflamme, G. Tabacchi, A. Glöß, M. Lass, I. Bethune, C. J. Mundy, C. Plessl, M. Watkins, J. VandeVondele, M. Krack, and J. Hutter, J. Chem. Phys. 152, 194103 (2020).
- ³³ W. Liang, C. T. Chapman, and X. Li, J. Chem. Phys. **134**, 184102 (2011).
- ³⁴X. Li, S. M. Smith, A. N. Markevitch, D. A. Romanov, R. J. Levis, and H. B. Schlegel, Phys. Chem. Chem. Phys. 7, 233 (2005).
- 35 Y. Shao, Z. Gan, E. Epifanovsky, A. T. Gilbert, M. Wormit, J. Kussmann, A. W. Lange, A. Behn, J. Deng, X. Feng et al., Mol. Phys. 113, 184 (2015).
- ³⁶Y. Zhu and J. M. Herbert, J. Chem. Phys. **148**, 044117 (2018).
- ³⁷K. Lopata and N. Govind, J. Chem. Theory Comput. 7, 1344 (2011).
- ³⁸ M. Valiev, E. Bylaska, N. Govind, K. Kowalski, T. Straatsma, H. Van Dam, D. Wang, J. Nieplocha, E. Apra, T. Windus, and W. de Jong, Comput. Phys. Commun. 181, 1477 (2010).
- ³⁹ M. A. L. Marques, A. Castro, G. F. Bertsch, and A. Rubio, Comput. Phys. Commun. 151, 60 (2003).
- ⁴⁰N. Tancogne-Dejean, M. J. T. Oliveira, X. Andrade, H. Appel, C. H. Borca, G. Le Breton, F. Buchholz, A. Castro, S. Corni, A. A. Correa, U. De Giovannini, A. Delgado, F. G. Eich, J. Flick, G. Gil, A. Gomez, N. Helbig, H. Hübener, R. Jestädt, J. Jornet-Somoza, A. H. Larsen, I. V. Lebedeva, M. Lüders, M. A. L. Marques, S. T. Ohlmann, S. Pipolo, M. Rampp, C. A. Rozzi, D. A. Strubbe, S. A. Sato, C. Schäfer, I. Theophilou, A. Welden, and A. Rubio, J. Chem. Phys. 152, 124119 (2020)
- ⁴¹C. Lian, M. Guan, S. Hu, J. Zhang, and S. Meng, Adv. Theory Simul. 1, 1800055 (2018).
- ⁴²J. Ren, E. Kaxiras, and S. Meng, Mol. Phys. **108**, 1829 (2010).
- ⁴³X. Andrade, C. D. Pemmaraju, A. Kartsev, J. Xiao, A. Lindenberg, S. Rajpurohit,
 L. Z. Tan, T. Ogitsu, and A. A. Correa, J. Chem. Theory Comput. 17, 7447 (2021).
 ⁴⁴F. Gygi, IBM J. Res. Dev. 52, 137 (2008).
- ⁴⁵E. W. Draeger and F. Gygi, "Qbox code, Qb@ll version," Lawrence Livermore National Laboratory.
- ⁴⁶A. Schleife, E. W. Draeger, V. M. Anisimov, A. A. Correa, and Y. Kanai, Comput. Sci. Eng. 16, 54 (2014).
- ⁴⁷ A. Schleife, E. W. Draeger, Y. Kanai, and A. A. Correa, J. Chem. Phys. 137, 22A546 (2012).
- ⁴⁸ M. C. Payne, M. P. Teter, D. C. Allan, T. A. Arias, and J. D. Joannopoulos, Rev. Mod. Phys. **64**, 1045 (1992).
- ⁴⁹ M. Fuchs and M. Scheffler, Comput. Phys. Commun. 119, 67 (1999).
- ⁵⁰ Y. Miyamoto, O. Sugino, and Y. Mochizuki, Appl. Phys. Lett. 75, 2915 (1999).
- ⁵¹D. Marx and J. Hutter, Ab Initio Molecular Dynamics: Basic Theory and Advanced Methods (Cambridge University Press, 2009).

- ⁵²O. Sugino and Y. Miyamoto, Phys. Rev. B **59**, 2579 (1999).
- ⁵³L. Lin, J. Chem. Theory Comput. **12**, 2242 (2016).
- ⁵⁴W. Kohn, Phys. Rev. Lett. **76**, 3168 (1996).
- 55 E. Prodan and W. Kohn, Proc. Natl. Acad. Sci. U. S. A. 102, 11635 (2005).
- ⁵⁶H.-Y. Ko, J. Jia, B. Santra, X. Wu, R. Car, and R. A. DiStasio, Jr., J. Chem. Theory Comput. **16**, 3757 (2020).
- ⁵⁷ M. Stengel and N. A. Spaldin, Phys. Rev. B **73**, 075121 (2006).
- ⁵⁸G. F. Bertsch, J.-I. Iwata, A. Rubio, and K. Yabana, *Phys. Rev. B* **62**, 7998 (2000).
- ⁵⁹QB@CH, Qbox at Chapel Hill, University of North Carolina at Chapel Hill, https://github.com/chrsshpr/QBACH.
- ⁶⁰ J. P. Perdew and W. Yue, Phys. Rev. B **33**, 8800 (1986).
- ⁶¹ A. D. Becke, J. Chem. Phys. **140**, 18A301 (2014).
- 62 A. D. Becke, J. Chem. Phys. 98, 5648 (1993).
- 63 A. J. Cohen, P. Mori-Sánchez, and W. Yang, Chem. Rev. 112, 289 (2012).
- 64 H. Eshuis and F. Furche, J. Phys. Chem. Lett. 2, 983 (2011).
- ⁶⁵ J. M. Yu, B. D. Nguyen, J. Tsai, D. J. Hernandez, and F. Furche, J. Chem. Phys. 155, 040902 (2021).
- ⁶⁶S. G. Balasubramani, V. K. Voora, and F. Furche, J. Chem. Phys. **157**, 164107 (2022).
- ⁶⁷J. P. Perdew and K. Schmidt, AIP Conf. Proc. 577, 1 (2001).
- ⁶⁸ J. P. Perdew, MRS Bull. **38**, 743–750 (2013).
- ⁶⁹P. Hohenberg and W. Kohn, Phys. Rev. **136**, B864 (1964).
- ⁷⁰ J. P. Perdew, K. Burke, and M. Ernzerhof, Phys. Rev. Lett. 77, 3865 (1996).
- 71 T. Aschebrock and S. Kümmel, Phys. Rev. Res. 1, 033082 (2019).
- 72 Y. Yao and Y. Kanai, J. Chem. Phys. 146, 224105 (2017).
- ⁷³R. Peverati and D. G. Truhlar, J. Phys. Chem. Lett. **2**, 2810 (2011).
- ⁷⁴J. Jaramillo, G. E. Scuseria, and M. Ernzerhof, J. Chem. Phys. 118, 1068 (2003).
- ⁷⁵D. A. Egger, S. Weissman, S. Refaely-Abramson, S. Sharifzadeh, M. Dauth, R. Baer, S. Kümmel, J. B. Neaton, E. Zojer, and L. Kronik, J. Chem. Theory Comput. 10, 1934 (2014).
- ⁷⁶D. Wing, G. Ohad, J. B. Haber, M. R. Filip, S. E. Gant, J. B. Neaton, and L. Kronik, Proc. Natl. Acad. Sci. U. S. A. 118, e2104556118 (2021).
- ⁷⁷ A. J. Garza and G. E. Scuseria, J. Phys. Chem. Lett. 7, 4165 (2016).
- ⁷⁸ J. Paier, M. Marsman, and G. Kresse, Phys. Rev. B **78**, 121201 (2008).
- ⁷⁹N. T. Maitra, J. Phys.: Condens. Matter **29**, 423001 (2017).
- ⁸⁰S. Refaely-Abramson, M. Jain, S. Sharifzadeh, J. B. Neaton, and L. Kronik, Phys. Rev. B 92, 081204 (2015).
- ⁸¹ P. Bleiziffer, A. Heßelmann, and A. Görling, J. Chem. Phys. 136, 134102 (2012).
- ⁸²W. Jia and L. Lin, Comput. Phys. Commun. **240**, 21 (2019).
- ⁸³ W. Hu, L. Lin, A. S. Banerjee, E. Vecharynski, and C. Yang, J. Chem. Theory Comput. 13, 1188 (2017).
- ⁸⁴J. Li, L. Wan, S. Jiao, W. Hu, and J. Yang, Electron. Struct. **5**, 014008 (2023).
- ⁸⁵N. Marzari and D. Vanderbilt, Phys. Rev. B **56**, 12847 (1997).
- ⁸⁶X. Wu, A. Selloni, and R. Car, Phys. Rev. B **79**, 085102 (2009).
- ⁸⁷E. Ditler, J. Mattiat, and S. Luber, Phys. Chem. Chem. Phys. 25, 14672 (2023).
- 88 R. Resta, Phys. Rev. Lett. 80, 1800 (1998).
- ⁸⁹ J. P. Perdew, M. Ernzerhof, and K. Burke, J. Chem. Phys. **105**, 9982 (1996).
- 90 A. Castro, M. A. L. Marques, and A. Rubio, J. Chem. Phys. 121, 3425 (2004).
- ⁹¹ D. R. Hamann, M. Schlüter, and C. Chiang, Phys. Rev. Lett. **43**, 1494 (1979).
- 92 P. Lautenschlager, M. Garriga, L. Vina, and M. Cardona, Phys. Rev. B $\mathbf{36},$ 4821 (1987).
- ⁹³Y.-M. Byun and C. A. Ullrich, Phys. Rev. B **95**, 205136 (2017).
- ⁹⁴J. Sun, C.-W. Lee, A. Kononov, A. Schleife, and C. A. Ullrich, Phys. Rev. Lett. 127, 077401 (2021).
- 95 D. Varsano, A. Marini, and A. Rubio, Phys. Rev. Lett. 101, 133002 (2008).
- ⁹⁶ J. Sun, A. Ruzsinszky, and J. P. Perdew, Phys. Rev. Lett. 115, 036402 (2015).
- ⁹⁷ P. J. Stephens, F. J. Devlin, C. F. Chabalowski, and M. J. Frisch, J. Phys. Chem. 98, 11623 (1994).
- 98 J. Heyd, G. E. Scuseria, and M. Ernzerhof, J. Chem. Phys. 118, 8207 (2003).
- ⁹⁹T. Yanai, D. P. Tew, and N. C. Handy, Chem. Phys. Lett. **393**, 51 (2004).
- ¹⁰⁰M. S. Hybertsen and S. G. Louie, Phys. Rev. Lett. **55**, 1418 (1985).
- ¹⁰¹G. Onida, L. Reining, and A. Rubio, Rev. Mod. Phys. **74**, 601 (2002).

- ¹⁰²D. Sangalli, A. Ferretti, H. Miranda, C. Attaccalite, I. Marri, E. Cannuccia, P. Melo, M. Marsili, F. Paleari, A. Marrazzo, G. Prandini, P. Bonfa, M. O. Atambo, F. Affinito, M. Palummo, A. Molina-Sánchez, C. Hogan, M. Grüning, D. Varsano, and A. Marini, J. Phys.: Condens. Matter 31, 325902 (2019).
- ¹⁰³ A. Marini, C. Hogan, M. Grüning, and D. Varsano, Comput. Phys. Commun. 180, 1392 (2009).
- ¹⁰⁴B. Hetényi, J. Phys. A: Math. Theor. **42**, 412003 (2009).
- ¹⁰⁵E. Valença Ferreira de Aragão, D. Moreno, S. Battaglia, G. L. Bendazzoli, S. Evangelisti, T. Leininger, N. Suaud, and J. Berger, Phys. Rev. B 99, 205144 (2019).
- ¹⁰⁶S. Evangelisti, F. Abu-Shoga, C. Angeli, G. L. Bendazzoli, and J. A. Berger, Phys. Rev. B **105**, 235201 (2022).
- $^{107}\mathrm{Q}.$ Wan, "First principles simulations of vibrational spectra of aqueous systems," Ph.D. thesis, The University of Chicago ProQuest Dissertations & Theses, Ann Arbor, 2015.
- ¹⁰⁸M. Stengel and N. A. Spaldin, Phys. Rev. B 75, 205121 (2007).
- ¹⁰⁹R. D. King-Smith and D. Vanderbilt, Phys. Rev. B 47, 1651 (1993).
- ¹¹⁰D. Vanderbilt and R. King-Smith, Phys. Rev. B 48, 4442 (1993).
- ¹¹¹P. Umari and A. Pasquarello, Phys. Rev. B **68**, 085114 (2003).
- ¹¹²K. Yabana, T. Nakatsukasa, J.-I. Iwata, and G. Bertsch, Phys. Status Solidi B 243, 1121 (2006).
- ¹¹³ J. Hekele, Y. Yao, Y. Kanai, V. Blum, and P. Kratzer, J. Chem. Phys. **155**, 154801 (2021).
- ¹¹⁴C. D. Pemmaraju, F. D. Vila, J. J. Kas, S. A. Sato, J. J. Rehr, K. Yabana, and D. Prendergast, Comput. Phys. Commun. **226**, 30 (2018).
- ¹¹⁵ M. Kuisma, A. Sakko, T. P. Rossi, A. H. Larsen, J. Enkovaara, L. Lehtovaara, and T. T. Rantala, Phys. Rev. B **91**, 115431 (2015).
- ¹¹⁶F. Ding, E. B. Guidez, C. M. Aikens, and X. Li, J. Chem. Phys. **140**, 244705 (2014).
- ¹¹⁷K.-M. Lee, K. Yabana, and G. F. Bertsch, J. Chem. Phys. **134**, 144106 (2011).
- ¹¹⁸E. Makkonen, T. P. Rossi, A. H. Larsen, O. Lopez-Acevedo, P. Rinke, M. Kuisma, and X. Chen, J. Chem. Phys. **154**, 114102 (2021).
- ¹¹⁹C. Müller, M. Sharma, and M. Sierka, J. Comput. Chem. **41**, 2573 (2020).
- ¹²⁰ M. R. Provorse and C. M. Isborn, Int. J. Quantum Chem. 116, 739 (2016).
- ¹²¹ N. T. Maitra, I. Souza, and K. Burke, Phys. Rev. B 68, 045109 (2003).
- ¹²² A. F. Starace, Phys. Rev. A 3, 1242 (1971).
- ¹²³ A. F. Starace, Phys. Rev. A 8, 1141 (1973).
- ¹²⁴T. C. Rensink and T. M. Antonsen, Phys. Rev. A **94**, 063407 (2016).
- ¹²⁵K. Hanasaki, Z. A. Ali, M. Choi, M. Del Ben, and B. M. Wong, J. Comput. Chem. 44, 980 (2023).
- ¹²⁶S. Ismail-Beigi, E. K. Chang, and S. G. Louie, Phys. Rev. Lett. **87**, 087402 (2001).
- 127 F. Tang, Z. Li, C. Zhang, S. G. Louie, R. Car, D. Y. Qiu, and X. Wu, Proc. Natl. Acad. Sci. U. S. A. 119, e2201258119 (2022).
- ¹²⁸Q. Xu, M. Del Ben, M. Sait Okyay, M. Choi, K. Z. Ibrahim, and B. M. Wong, J. Chem. Theory Comput. **19**, 7989 (2023).
- ¹²⁹P. Umari and A. Pasquarello, Phys. Rev. Lett. 89, 157602 (2002).
- ¹³⁰R. Rodrigues Pela and C. Draxl, Electron. Struct. 3, 037001 (2021).
- ¹³¹T. Otobe, K. Yabana, and J.-I. Iwata, J. Phys.: Condens. Matter 21, 064224 (2009).
- 132 G. J. Martyna and M. E. Tuckerman, J. Chem. Phys. 110, 2810 (1999).
- ¹³³N. D. M. Hine, J. Dziedzic, P. D. Haynes, and C.-K. Skylaris, J. Chem. Phys. 135, 204103 (2011).
- ¹³⁴O. Andreussi and N. Marzari, Phys. Rev. B **90**, 245101 (2014).
- ¹³⁵U. De Giovannini, A. H. Larsen, and A. Rubio, Eur. Phys. J. B 88, 56 (2015).
- $^{136}\mathrm{P}.$ Wopperer, U. De Giovannini, and A. Rubio, Eur. Phys. J. B 90,~51~(2017).
- ¹³⁷J. G. Muga, J. P. Palao, B. Navarro, and I. L. Egusquiza, Phys. Rep. **395**, 357 (2004).
- ¹³⁸A. Kononov, C.-W. Lee, T. P. dos Santos, B. Robinson, Y. Yao, Y. Yao, X. Andrade, A. D. Baczewski, E. Constantinescu, A. A. Correa et al., MRS Commun. 12, 1002 (2022).
- ¹³⁹U. De Giovannini, H. Hübener, and A. Rubio, J. Chem. Theory Comput. 13, 265 (2017).